

Site-Specific Chemical Doping Reveals Electron Atmospheres at the Surfaces of Organic Semiconductor Crystals

Tao He

Shandong University

Matthias Stolte

Universität Würzburg

Yan Wang

University of Minnesota

Rebecca Renner

University of Würzburg

Paul Ruden

University of Minnesota

Frank Würthner

University of Würzburg <https://orcid.org/0000-0001-7245-0471>

C. Daniel Frisbie (✉ frisbie@umn.edu)

University of Minnesota

Article

Keywords: Electron Transport, Doping-induced Space Charge, Crystallographic Step Edges, Electron Traps, Field Effect Electron Mobility, Temperature Dependent Behavior

Posted Date: January 8th, 2021

DOI: <https://doi.org/10.21203/rs.3.rs-140330/v1>

License: © ⓘ This work is licensed under a Creative Commons Attribution 4.0 International License.

[Read Full License](#)

Abstract

Chemical doping controls the electronic properties of organic semiconductors, but so far, doping protocols and mechanisms are less developed than in conventional semiconductors. Here we describe a unique, site-specific, n-type surface doping mechanism for single crystals of two benchmark organic semiconductors that produces dramatic improvement in electron transport and concurrently provides unprecedented evidence for doping-induced space charge. The surface doping chemistry specifically targets crystallographic step edges, which are known electron traps, simultaneously passivating the traps and releasing itinerant electrons. The effect on electron transport is profound: field effect electron mobility increases by as much as a factor of 10 and its temperature dependent behavior switches from thermally-activated to band-like. Our findings suggest new site-specific strategies to dope organic semiconductors that differ from the conventional redox chemistry of randomly distributed substitutional impurities. Critically, they also verify the presence of dopant-induced electron atmospheres, confirming long-standing expectations for organic systems from conventional solid-state theory.

Main Text

Chemical doping plays a central role in the science and applications of organic semiconductor materials¹⁻⁶. Decades ago, the discovery that crystals and films of pi-conjugated molecules could be made highly conducting, and even metallic, by chemical doping (e.g., conducting polymers) sparked world-wide interest in these materials and marked a critical turning point in the field of organic electronics⁷⁻¹³. Today, p- and n-type doping of organic semiconductor films is employed industrially to lower the operating voltages of organic light-emitting diode (OLED) displays^{1,14,15}. Still, many structural and electronic aspects of chemical doping in organic semiconductors remain poorly understood, particularly for crystalline or polycrystalline systems where strong anisotropic intermolecular interactions, crystalline defects, and microstructure can be decisive in determining the doping mechanism and ionization efficiency¹⁶⁻²¹.

Here we report two discoveries related to chemical doping of organic semiconductors. First, we have found that crystallographic step-edges on the surfaces of specific organic semiconductor crystals can be selectively n-doped. Remarkably, this site-specific doping eliminates shallow electron traps at the step edges and results in dramatic recovery of band-like transport properties for crystals that, prior to doping, had low field-effect electron mobilities and strongly activated (trap-limited) transport. This intriguing result suggests site-specific doping may be a productive new strategy for improved material performance in organic electronics. Second, we have discovered that doping-induced electron atmospheres along the step edges can be visualised by scanning Kelvin probe microscopy (SKPM). To our knowledge, the striking SKPM images represent the first direct detection of space charge associated with chemical doping in an organic semiconductor and thus provide critical verification of doping effects in organic systems that match expectations from classical inorganic semiconductor physics.

Collectively, these findings advance the fundamental understanding of chemical doping in crystalline organic systems and provide a poignant demonstration of the capacity of transport measurements combined with high resolution Kelvin probe microscopy for uncovering critical structure-transport relationships²². A significant additional revelation is that the quasi-one-dimensional (1D) nature of the step-edge doping affords an excellent testbed for quantitative analysis of SKPM potential images, which we have utilized to develop a more comprehensive understanding of SKPM for semiconductor characterization.

Our study focuses on crystals of Cl₂-NDI^{23,24} (space group P-1) and PDIF-CN₂^{25,26} (space group P-1), respectively, Figure 1, well-known semiconducting materials that exhibit outstanding n-channel performance in field-effect transistors (FETs). Exposure of the (001) surfaces of both crystals to an N-silane vapor ([3-(2-aminoethylamino)propyl]trimethoxysilane, Figure 1a) results in n-type doping that is evident in FET measurements, as described below. Our motivation to use this amine as a dopant was based in part on the known redox reactivity of Cl₂-NDI and PDIF-CN₂ with amines, and in part on trial-and-error experiments with a variety of different amines (see Supplementary Fig. 1-3)²⁷⁻³¹. Spectroelectrochemistry and UV/Vis titration studies confirm that the N-silane in Figure 1a reduces Cl₂-NDI and PDIF-CN₂ in solution (Supplementary Fig. 4, 5), and we hypothesized that spontaneous electron transfer from the amines to the crystals could produce n-type surface doping.

To test this hypothesis, we grew lath-like crystals of Cl₂-NDI and PDIF-CN₂ with thicknesses ranging from 1-50 μm by physical vapor transport and laminated the crystals onto Au-coated polydimethylsiloxane (PDMS) stamps to make four terminal “air-gap” FETs (Figure 1a)^{26,32}. In these FETs, the empty space, typically air or vacuum, between the recessed gate and the crystal surface forms the gate dielectric. Such devices have the advantage that the gated semiconductor surface is pristine. The transport characteristics of the completed crystal FETs were then measured under vacuum. Subsequently, doping of the same crystals was accomplished by exposing the FETs to the N-silane vapor using the quartz hot wall apparatus shown schematically in Figure 1a. Contact of the N-silane vapor with the crystal face forming the FET channel was possible because of the air gap FET design.

Figure 2a shows representative FET drain current-gate voltage (I_D - V_G) characteristics for a relatively thick (47 μm) Cl₂-NDI crystal before and after exposure to 100 μL of N-silane. (For all FET results the source is grounded, i.e., $V_S = 0$). The un-doped, as-grown crystal exhibits n-type field effect conduction as expected (i.e., turning ON as V_G becomes more positive), and after exposure to the N-silane there is a clear negative shift in the onset voltage, as well as improvement of the maximum conductance in the ON state. Note for example that at $V_G = 0$ V, I_D is five orders of magnitude greater after doping. The drain current-drain voltage (I_D - V_D) characteristics also reveal substantial differences, Figure 2b. After doping, the crystal does not show characteristic current saturation, and the currents at the same V_G and V_D values are more than an order of magnitude higher than for the same crystal prior to doping. The transport results in Figures 2a and 2b clearly indicate n-type doping for the thick Cl₂-NDI crystal. However, *thin* (2.9 μm) Cl₂-NDI crystal

results are much different, Supplementary Fig. 6. Exposure of thin crystals to the N-silane does not produce a large onset voltage shift, nor does it result in any significant change in maximum ON current. There is only a change in the OFF current (i.e., at negative V_G values). The results in Figure 2a and Supplementary Fig. 6 are representative of many experiments on thick and thin crystals. Evidently, crystal thickness somehow plays a vital role in the doping effect. We carried out the same doping experiments with PDIF-CN₂ crystals and found essentially the same results (see Supplementary Fig. 7).

We have shown previously that the crystallographic step edge density on the (001) surface of as-grown Cl₂-NDI and PDIF-CN₂ crystals is highly correlated with crystal thickness^{24,33}. Furthermore, we have demonstrated that the step edges, Figure 1c, serve as electron traps in FET measurements. It therefore seemed reasonable that the doping effects were actually directly related to step density, rather than crystal thickness. Figure 1d shows atomic force microscopy (AFM) images of one unit cell tall steps on both the thick and thin crystals (note the difference in scale bars). Figure 2c displays ON state sheet conductance σ_s at $V_G = +60$ V for a large number of as-grown (93) and doped (64) Cl₂-NDI and PDIF-CN₂ crystals as a function of step density. For as-grown Cl₂-NDI and PDI-CN₂ crystals, σ_s decreases strongly with step density. However, the dependence is opposite for doped crystals. For doped crystals, σ_s *increases* with step density. These trends do not reflect changes in contact resistance upon doping as the contact resistance in these devices is small relative to the channel resistance (see Supplementary Fig. 8). The FET threshold voltages V_T shown in Figure 2d also trend oppositely for as-grown vs. doped samples. For as-grown crystals, V_T becomes more positive with increasing step density, consistent with step edge trapping that we have reported previously²⁴. For doped crystals, V_T is increasingly *negative* as step density increases, i.e., turning the FET channel OFF requires strongly negative gate voltages, consistent with increased n-doping as step density increases. The data in panels c and d are indeed consistent with the critical role of step edges in the doping mechanism. Definitive resolution of whether crystal thickness or surface step edge density is the key factor in the doping mechanism – as the two structural characteristics are proportional to each other – is presented below, but first we complete the discussion of transport effects.

The temperature dependences of the FET I_D - V_G characteristics for the *same* Cl₂-NDI crystal in its as-grown and doped states, respectively, are shown in Figures 3a and 3b. The linear regime electron mobility and threshold voltages extracted from these traces are displayed in Figures 3c and 3d (see also Supplementary Fig. 9 for V_G dependence of mobility). The doped crystal exhibits a factor of 10 higher room temperature electron mobility, and importantly, the mobility increases as temperature decreases, reaching 9.4 cm²/Vs at 150 K, which is indicative of band-like transport. For the as-grown crystal the mobility is significantly lower at all temperatures and clearly thermally activated, consistent with trapping. The profoundly different μ - T behavior in Figure 3c suggest substantial reduction of shallow traps on the surface of the doped crystal³⁴⁻³⁶. The V_T behavior is also consistent with this interpretation. For the doped crystal, the slope of the V_T - T correlation is 2-3 times smaller than the corresponding slope for the same crystal in its as-grown state, and V_T is only a few volts even at 150 K for the doped version, whereas

it is tens of volts for the as-grown case (Fig. 3d and Supplementary Fig. 10). The smaller V_T values and the weaker temperature dependence are consistent with less trapping for the doped crystal^{37,38}. Together, the μ and V_T behavior thus reveal a strong qualitative improvement in the transport behavior for Cl₂-NDI crystals upon doping. Again, similar observations were made for as-grown and doped PDIF-CN₂ crystals (see Supplementary Fig. 11). Furthermore, pronounced band-like charge transport was observed in all doped devices, regardless of thickness or step density, which was in sharp contrast to the as-grown crystals that displayed band-like behavior only for the very thinnest crystals, that is, those with the lowest step densities (see Figure 2c). We note also that the doped devices were quite stable. Mobilities for devices stored in air for two months degraded by only ~18% (Supplementary Fig. 12 and Fig. 13).

We turn now to the mechanism of n-doping. The size of the N-silane molecule and the tight-packing of the Cl₂-NDI and PDIF-CN₂ crystals suggested to us that the doping mechanism was a surface, not a bulk, phenomenon, as has been reported before for fluoroalkyl silane surface doping of rubrene crystals^{16,39}. To prove this point we carried out depth profiling experiments to measure the concentration of N-silane as a function of depth into the crystal. The data indicate that indeed the N-silane does not penetrate into the bulk of the crystal, but is confined to the surface, as expected (Supplementary Fig. 14). Additionally, X-ray diffraction revealed no evidence of crystal expansion after doping (Supplementary Fig. 15)^{18,40}.

To understand the surface effects of N-silane exposure, we undertook scanning probe microscopy analysis of the crystal surfaces. Figures 4a and 4c show topographic AFM images of the Cl₂-NDI and PDIF-CN₂ surfaces after N-silane doping. A clear ridge, several nm high, is evident at each step edge. Such ridges are not evident in untreated crystals, indicating the N-silane selectively interacts with molecules at the step edges (see another example in Supplementary Fig. 16). As noted already, N-silane readily undergoes electron transfer reactions with Cl₂-NDI and PDIF-CN₂ in solution to make the corresponding radical anions (Supplementary Fig. 4, 5). This is illustrated for the case of Cl₂-NDI in Figure 5a, which shows the UV/Vis absorption spectra for Cl₂-NDI upon spectroelectrochemical reduction in solution in comparison to the observations for a thin film of Cl₂-NDI exposed to N-silane. The bands at ~ 480 nm, 520 nm and 600 nm are clear signatures of the Cl₂-NDI radical anion (see Supplementary Fig. 4)⁴¹. Similar results are obtained for PDIF-CN₂ in solution (see Supplementary Fig. 5). For the crystals, we speculate that N-silane can reduce Cl₂-NDI and PDIF-CN₂ molecules located at the step edges because the redox-active pi-cores of the molecules are exposed on the step faces (see Figure 1c). In contrast, the crystalline terraces, which correspond to the (001) planes, are terminated with fluoroalkyl chains that effectively block molecular interaction and electron transfer. Thus, it is the unit cell structure of Cl₂-NDI and PDIF-CN₂ crystals, combined perhaps with the less aggressive reducing power of the N-silane, which provides the step edge specificity of the doping chemistry. Silanes are known to undergo oligomerization, and once reaction has occurred at the step edge further reactions may follow to create a several nm thick N-silane multilayer stripe as shown in Figures 4a and 4c⁴².

Significantly, the SKPM images in Figures 4b and 4d, which correspond to the topographic images in Figures 4a and 4c, show striking electric potential contrast^{39,43}. Coincident with each step edge for both doped crystals, positive and negative potential stripes are clearly evident. In particular, one sees that the positive stripe at each step edge is flanked by negative potential stripes on either side. Insets to the panels show line scans across the step edge potential stripes. From the profile in Figure 4c for Cl₂-NDI, it is evident that the peak positive potential is ~+50 mV and the peak negative potential exceeds -100 mV, both very large values. The total width of the entire stripe is nearly 5 μm. For PDIF-CN₂ in Figure 4d, the results are quite similar with the exception that the peak negative potentials are even lower, i.e., less than -300 mV. In our prior work on undoped crystals, only positive SKPM potentials were observed at step edges²⁴. Thus, the potential signatures measured at the step edges have completely changed after treatment with the N-silane. The interpretation of these potentials requires some care as will become evident in the discussion below. Importantly, to assess the robustness of the Figure 4 results, we have carried out many SKPM experiments under different scanning conditions and modes (e.g. amplitude modulation vs. frequency modulation). While the precise potentials observed in Figure 4 depend on tip lift height and AC bias, the overall “triple stripe” pattern at the step edges is always observed for doped crystals, and it is distinct from the step edge potential measured for undoped samples (see Supplementary Figs. 17-30).

We also undertook ultraviolet photoelectron spectroscopy (UPS) measurements of doped crystals with high step densities to confirm our interpretation of the effects of N-silane exposure. UPS is a classical technique for examining band alignment in doped semiconductors⁴⁴⁻⁴⁷ and in this case it also has the advantage that it averages over a geometrical area much larger than the distances between steps and so provides complementary information to SKPM. Figure 5b compares the UPS results for doped and as-grown Cl₂-NDI crystals in the valence (HOMO) band and photoelectron cut-off regions (see also Supplementary Fig. 31). It is clear that the surface-doped Cl₂-NDI crystals display both a 0.3 eV deeper HOMO and a 0.5 eV smaller work function (higher binding energy at cut-off). These results are depicted in the energy level diagram on the right side of Figure 5b. Positive ionization of the N-silane by electron donation to sub-surface layers of the crystal results in an effective dipole at the crystal surface that lowers the work function (i.e., creates a downward vacuum level shift), consistent with the UPS observation. Likewise, a higher HOMO binding energy relative to the Fermi level for the doped crystal is indicative of a downward shift in the LUMO and HOMO energies and thus indeed reflects n-doping (the LUMO-to-Fermi level offset is reduced). Thus, the UPS data in Figure 5b are consistent with the n-type step-edge doping mechanism.

From our collective experiments, an explanation for the potential images in Figures 4b and 4d thus emerges; we conclude that ionized donors, localized at the step edges, create a line of positive space-charge that is then screened by both the crystal dielectric response and itinerant, Coulombically-bound electrons, as shown schematically in Figure 5c. The electron distribution gives rise to the diffuse negative space-charge regions in the terraces bordering the positive line charge. It is this triple stripe space charge distribution at each step edge that is captured by the SKPM potential images. To our knowledge, the

images in Figures 4b and 4d are the first direct visualization of microscopic, doping-induced space charge in organic semiconductors.

However, there is an apparent difficulty with this interpretation, and that is that such a space charge distribution depicted in Figure 5c would be expected to yield a single positive peak in the surface potential profile across the doped step edge. A simulation of the expected potential profile is shown in Supplementary Fig. 35. Such a symmetric, monotonic profile is clearly not what is observed in Figures 4b and 4d.

At this point, we must carefully consider what is measured in the SKPM experiment. Critically, we note that the SKPM probe is only sensitive to the perpendicular (z) component of the electric field emanating from the surface; the parallel (x, y) components of the electric field do not produce a force that can be sensed. With this in mind, we developed a simple, macroscopic equilibrium electrostatics model that allows for non-linear screening by mobile electrons in the semiconductor (Supplementary Fig. 33). In the simulation, the doped step edge was modeled as an infinite, straight, positive line charge along the y -axis on the planar interface between air and the semiconductor. The semiconductor is characterized by its dielectric response and an induced electron population that screened the positive line charge. Simulation details can be found in the Supporting Information, and a plot of the calculated electric field distribution in the x - z plane is shown in Supplementary Fig. 34.

In the SKPM experiment, the probe runs along a trace above the semiconductor, where the electric field decays relatively slowly with distance from the line charge. The force on the probe tip perpendicular to the sample surface tracks the z -component of the field, E_z , where z is the tip-to-surface distance. To counter this force, an electrochemical potential is applied between the probe and the semiconductor sample. Since the spatial resolution is limited by the probe tip size (with a typical radius of curvature of 50 nm), we performed a convolution of the calculated field distribution, E_z , with a Gaussian of width comparable to the expected resolution. The results of the simulation are shown in Figure 5d.

Importantly, the simulated E_z profiles for several different tip-to-surface distances in Figure 5d account very nicely for the shape of the measured spatial SKPM profiles in Figures 4b and 4d. In particular, the macroscopic length scale of the measured profiles agrees with the simulated spatial extent of the induced electron density in the semiconductor near the positive surface line charge. We note that quantitative comparison of the simulated profiles with our SKPM data is not possible due to the assumptions and simplifications that entered the model, but the main point is confirmed, namely that the SKPM images are due to an intriguing triple stripe space charge distribution at the crystal step edges.

We note that another conclusion of our analysis is that the potentials in the SKPM images are not true surface potentials. This is certainly an important point to bear in mind in considering comparisons of the SKPM potentials to other energy scales, such as trap energies or electron mobility activation energies. Still, it is clear in this case that the SKPM potentials measured in Figure 4 are large and they represent an underestimate of the true surface potential due to the space charge. It can also be anticipated that the

potential corrugation evident for doped Cl₂-NDI and PDIF-CN₂ crystals must diminish substantially in FETs upon application of gate fields that increase the overall carrier concentration. If this were not the case, the potential variations would lead to significant carrier scattering effects.

In conclusion, we have discovered a site-specific n-type doping mechanism on the surfaces of single crystals of two benchmark organic semiconductors. The site-specific doping eliminates electron traps and increases the background electron concentration, which in turn leads to superior ON-state conductances for FETs based on the doped crystals. The novelty of the doping mechanism is that it targets specific, well-defined structural features on the surfaces of the crystals – namely step edges – that have been shown to be detrimental to transport. To our knowledge, this is the first such example of site-specific doping in crystalline organic semiconductors and it offers the intriguing possibility of a general strategy in which targeted doping chemistry selectively “erases” the effects of well-defined trap states. A general strategy of course hinges on continued identification of other well-defined structural features, such as grain boundaries, that serve as charge traps in crystalline organic materials, and specific doping chemistry that can address them.

Our study has also shown the first images of dopant-induced space charge in organic semiconductor crystals. The importance of this for organic semiconductor science is that it provides expected but gratifying confirmation that the classical picture of doping in conventional semiconductors applies well to organic systems. Specifically, the SKPM images show that electrons released into the host crystal by ionized donors are mobile and are able to delocalize subject (essentially) only to the Coulomb potential associated with the spatially localized, ionized donors. We anticipate that site-specific chemical doping demonstrated here, in combination with SKPM imaging, can be a powerful approach for further understanding of doping effects and defects in crystalline organic semiconductor systems.

Method

Materials. Cl₂-NDI was synthesized according to the literature⁴⁸. PDIF-CN₂ is commercially available from Flexterra Inc. (Polyera Activink N1100). All dopants were purchased from Sigma-Aldrich.

Four-terminal FET fabrication. As described previously, high-quality single crystals were grown by the physical vapor transport (PVT) method and then laminated onto a pre-patterned Au-coated PDMS substrate featuring source, drain, gate and channel electrodes to make a four-terminal FET. The crystal long-axis corresponding to pi-stacking direction was aligned perpendicular to the source and drain electrodes as shown in Figure 1^{24,26}. All contact electrodes consisted of a Cr (3 nm) /Au (20 nm) bilayer film. The distance between the source and drain electrodes was 300 μm and the distance between the two channel measurement electrodes (V₁ and V₂) was 150 μm. The gate-to-crystal gap was 5 μm for all devices. The specific capacitance of the crystal-gap-gate stack is 0.18 nF/cm². The I-V characteristics of the devices were measured in an N₂-filled glove box and variable temperature measurements were carried out in the dark with a cryogenic probe station at 10⁻⁴ Torr.

N-silane doping. To carry out doping, a single crystal FET was removed from the FET probe station and placed in the quartz doping vessel along with a small glass dish containing a well-defined volume of the N-silane liquid (typically 50-300 μL depending on the desired dose). The vessel was closed and evacuated to 0.1 Torr. A small Ar flow was established and then the walls of the vessel were heated resistively. The wall temperature surrounding the dopant dish was increased to 80 $^{\circ}\text{C}$ and the wall temperature of the device end of the vessel was heated to 50 $^{\circ}\text{C}$. After 1 h the liquid in the dish was completely evaporated, the N-silane was purged by increasing the Ar gas flow, and the apparatus was cooled. The treated FET was removed and transferred back to the vacuum probe station for electrical measurements.

Molecular characterization. $^1\text{H-NMR}$ spectra were recorded with a Bruker 400 MHz spectrometer. UV/Vis absorption spectra were recorded with a Spectronic Genesys spectrometer in transmission mode. Spectra of the radical anions were recorded in reflection mode using a three-electrode custom-made electrochemical cell inserted in an Agilent Cary 5000 UV/Vis/NIR spectrometer (Electrolyte was 0.1 M Bu_4NPF_6 in dry CHCl_3 , with 6 mm Pt-disc working electrode, Pt counter and Ag/AgCl leak free reference electrode (Warner Instruments)). The optical path was adjusted to 100 μm with a micrometer screw. Potentials were applied with a reference 600 potentiostat (Gamry Instruments). Application of potential steps and recording of absorption spectra was automated by a Lab View routine.

X-ray Diffraction and XPS/UPS analysis. High-resolution X-ray diffraction (XRD) was carried out with a Philips Panalytical X'Pert Pro diffractometer with monochromatic Cu K α radiation (wavelength 0.154 nm) at tube settings of 45 kV and 40 mA. X-ray photoelectron spectra (XPS) and ultraviolet photoelectron spectroscopy (UPS) were taken on an PHI VersaProbe III (10^{-8} Torr) equipped with a hemispherical analyzer, using an Al K α X-ray monochromatic source (1486.6 eV) and He discharge lamp ($h\nu(\text{He I})=21.22$ eV) as excitation sources, respectively. For XPS, the X-ray anode was operated at 200 W, and the analyzer was set to a pass energy of 280 eV for survey scans and 112 eV for high-resolution scans. The samples were prepared, stored and transferred under N_2 atmosphere until introduced to the measurement apparatus.

Scanning Kelvin probe microscopy. Measurements were performed with a Bruker Instruments Nanoscope V Multimode AFM with conductive probes from Mikromasch USA (NSC18, Pt coated, resonant frequency 60 - 90 kHz, $k = 2\text{-}5.5$ N/m, $R_C = 25$ nm). All SKPM topography and potential scans were conducted with a tip AC voltage $V_{AC} = 6$ V and lift height $d = 10$ nm inside an Ar-filled glovebox with oxygen levels (~ 1 ppm) to mitigate surface contamination effects.

References

1. Walzer, K., Maennig, B., Pfeiffer, M. & Leo, K. Highly Efficient Organic Devices Based on Electrically Doped Transport Layers. *Chem. Rev.* **107**, 1233-1271 (2007).
2. Lussem, B. *et al.* Doped Organic Transistors. *Chem. Rev.* **116**, 13714-13751 (2016).
3. Xu, Y. *et al.* Doping: A Key Enabler for Organic Transistors. *Adv. Mater.* **30**, 1801830 (2018).

4. Kang, K. *et al.* 2D coherent charge transport in highly ordered conducting polymers doped by solid state diffusion. *Nat. Mater.* **15**, 896 (2016).
5. Lin, X. *et al.* Beating the thermodynamic limit with photo-activation of n-doping in organic semiconductors. *Nat. Mater.* **16**, 1209-1215 (2017).
6. Yamashita, Y. *et al.* Efficient molecular doping of polymeric semiconductors driven by anion exchange. *Nature* **572**, 634-638 (2019).
7. Bolto, B. A., McNeill, R. & Weiss, D. E. Electronic Conduction in Polymers. III. Electronic Properties of Polypyrrole. *Aust. J. Chem.* **16**, 1090-1103 (1963).
8. Shirakawa, H., Louis, E. J., MacDiarmid, A. G., Chiang, C. K. & Heeger, A. J. Synthesis of electrically conducting organic polymers: halogen derivatives of polyacetylene, (CH)_x. *J. Chem. Soc., Chem. Commun.* 578-580 (1977).
9. Baughman, R. H., Bredas, J. L., Chance, R. R., Elsenbaumer, R. L. & Shacklette, L. W. Structural basis for semiconducting and metallic polymer dopant systems. *Chem. Rev.* **82**, 209-222 (1982).
10. Garito, A. F. & Heeger, A. J. Design and synthesis of organic metals. *Acc. Chem. Res.* **7**, 232-240 (1974).
11. Chiang, C. K. *et al.* Electrical Conductivity in Doped Polyacetylene. *Phys. Rev. Lett.* **39**, 1098-1101 (1977).
12. Ferraris, J., Cowan, D. O., Walatka, V. & Perlstein, J. H. Electron transfer in a new highly conducting donor-acceptor complex. *J. Am. Chem. Soc.* **95**, 948-949 (1973).
13. Bryce, M. R. Recent progress on conducting organic charge-transfer salts. *Chem. Soc. Rev.* **20**, 355-390 (1991).
14. Huang, J. *et al.* Low-voltage organic electroluminescent devices using pin structures. *Appl. Phys. Lett.* **80**, 139-141 (2002).
15. Zhou, X. *et al.* Very-low-operating-voltage organic light-emitting diodes using a p-doped amorphous hole injection layer. *Appl. Phys. Lett.* **78**, 410-412 (2001).
16. Calhoun, M. F., Sanchez, J., Olaya, D., Gershenson, M. E. & Podzorov, V. Electronic functionalization of the surface of organic semiconductors with self-assembled monolayers. *Nat. Mater.* **7**, 84-89 (2008).
17. Alves, H., Molinari, A. S., Xie, H. & Morpurgo, A. F. Metallic conduction at organic charge-transfer interfaces. *Nat. Mater.* **7**, 574-580 (2008).
18. Duong, D. T., Wang, C., Antono, E., Toney, M. F. & Salleo, A. The chemical and structural origin of efficient p-type doping in P3HT. *Org. Electron.* **14**, 1330-1336 (2013).
19. Han, Y. *et al.* Anion-induced N-doping of naphthalenediimide polymer semiconductor in organic thin-film transistors. *npj Flex. Electron.* **2**, 11 (2018).
20. Lu, G. *et al.* Moderate doping leads to high performance of semiconductor/insulator polymer blend transistors. *Nat. Commun.* **4**, 1588 (2013).
21. Olthof, S. *et al.* Ultralow Doping in Organic Semiconductors: Evidence of Trap Filling. *Phys. Rev. Lett.* **109**, 176601 (2012).

22. Bürgi, L., Richards, T., Chiesa, M., Friend, R. H. & Sirringhaus, H. A microscopic view of charge transport in polymer transistors. *Synth. Met.* **146**, 297-309 (2004).
23. He, T. *et al.* Single-crystal field-effect transistors of new Cl₂-NDI polymorph processed by sublimation in air. *Nat. Commun.* **6**, 5954 (2015).
24. He, T. *et al.* Crystal step edges can trap electrons on the surfaces of n-type organic semiconductors. *Nat. Commun.* **9**, 2141 (2018).
25. Jones, B. A. *et al.* High-mobility air-stable n-type semiconductors with processing versatility: dicyanoperylene-3,4:9,10-bis(dicarboximides). *Angew. Chem. Int. Ed.* **43**, 6363-6366 (2004).
26. Minder, N. A., Ono, S., Chen, Z., Facchetti, A. & Morpurgo, A. F. Band-like electron transport in organic transistors and implication of the molecular structure for performance optimization. *Adv. Mater.* **24**, 503-508 (2012).
27. Russ, B. *et al.* Tethered tertiary amines as solid-state n-type dopants for solution-processable organic semiconductors. *Chem. Sci.* **7**, 1914-1919 (2016).
28. Park, J. *et al.* Single-gate bandgap opening of bilayer graphene by dual molecular doping. *Adv. Mater.* **24**, 407-411 (2012).
29. Lee, B. H., Bazan, G. C. & Heeger, A. J. Doping-Induced Carrier Density Modulation in Polymer Field-Effect Transistors. *Adv. Mater.* **28**, 57-62 (2016).
30. Röger, C. & Würthner, F. Core-Tetrasubstituted Naphthalene Diimides: Synthesis, Optical Properties, and Redox Characteristics. *J. Org. Chem.* **72**, 8070-8075 (2007).
31. Kishore, R. S. K. *et al.* Ordered and Oriented Supramolecular n/p-Heterojunction Surface Architectures: Completion of the Primary Color Collection. *J. Am. Chem. Soc.* **131**, 11106-11116 (2009).
32. Sundar, V. C. *et al.* Elastomeric Transistor Stamps: Reversible Probing of Charge Transport in Organic Crystals. *Science* **303**, 1644-1646 (2004).
33. Kim, J. J. *et al.* Correlating Crystal Thickness, Surface Morphology, and Charge Transport in Pristine and Doped Rubrene Single Crystals. *ACS Appl. Mater. Interfaces* **10**, 26745-26751 (2018).
34. Materials, D. *et al.* Simulation of Temperature-Dependent Charge Transport in Organic Semiconductors with Various Degrees of Disorder. *J Chem. Theory Comput.* **12**, 3087-3096 (2016).
35. Podzorov, V. *et al.* Intrinsic charge transport on the surface of organic semiconductors. *Phys. Rev. Lett.* **93**, 086602 (2004).
36. Mei, Y. *et al.* Crossover from band-like to thermally activated charge transport in organic transistors due to strain-induced traps. *Proc. Natl. Acad. Sci. USA* **114**, 6739-6748 (2017).
37. Xie, H., Alves, H. & Morpurgo, A. F. Quantitative analysis of density-dependent transport in tetramethyltetraselenafulvalene single-crystal transistors: Intrinsic properties and trapping. *Phys. Rev. B* **80** (2009).
38. Zuo, G. *et al.* Molecular Doping and Trap Filling in Organic Semiconductor Host-Guest Systems. *J. Phys. Chem. C* **121**, 7767-7775 (2017).

39. Ellison, D. J., Lee, B., Podzorov, V. & Frisbie, C. D. Surface potential mapping of SAM-functionalized organic semiconductors by Kelvin probe force microscopy. *Adv. Mater.* **23**, 502-507 (2011).
40. Kleemann, H. *et al.* Structural phase transition in pentacene caused by molecular doping and its effect on charge carrier mobility. *Org. Electron.* **13**, 58-65 (2012).
41. Guha, S., Goodson, F. S., Corson, L. J. & Saha, S. Boundaries of Anion/Naphthalenediimide Interactions: From Anion- π Interactions to Anion-Induced Charge-Transfer and Electron-Transfer Phenomena. *J. Am. Chem. Soc.* **134**, 13679-13691 (2012).
42. Chauhan, A. K. *et al.* Self-assembly of the 3-aminopropyltrimethoxysilane multilayers on Si and hysteretic current-voltage characteristics. *Appl. Phys. A* **90**, 581-589 (2007).
43. Tello, M., Chiesa, M., Duffy, C. M. & Sirringhaus, H. Charge Trapping in Intergrain Regions of Pentacene Thin Film Transistors. *Adv. Funct. Mater.* **18**, 3907-3913 (2008).
44. Winkler, S. *et al.* Probing the energy levels in hole-doped molecular semiconductors. *Mater. Horiz.* **2**, 427-433 (2015).
45. Lussem, B. *et al.* Doped organic transistors operating in the inversion and depletion regime. *Nat. Commun.* **4**, 2775 (2013).
46. Mendez, H. *et al.* Charge-transfer crystallites as molecular electrical dopants. *Nat. Commun.* **6**, 8560 (2015).
47. Salzmann, I. *et al.* Intermolecular Hybridization Governs Molecular Electrical Doping. *Phys. Rev. Lett.* **108**, 035502 (2012).
48. Oh, J. H. *et al.* High-Performance Air-Stable n-Type Organic Transistors Based on Core-Chlorinated Naphthalene Tetracarboxylic Diimides. *Adv. Funct. Mater.* **20**, 2148-2156 (2010).

Declarations

Acknowledgements

This work was supported primarily by the MRSEC program of the National Science Foundation under Grant Number DMR-2011401. C.D.F. also acknowledges partial support from NSF DMR-1806419. Parts of this work were carried out in the College of Science and Engineering Characterization Facility, University of Minnesota, which has received capital equipment funding from the NSF through the UMN MRSEC program under Award Number DMR-2011401, and in the Minnesota Nano Center which is supported by NSF through the National Nano Coordinated Infrastructure (NNCI) Network, under Award Number ECCS-2025124. Parts of this work were also carried out at the Center for Nanosystems Chemistry at the Universität Würzburg, which has received funds from the Bavarian State Ministry of Science and Arts in the framework of the research program "Solar Technologies Go Hybrid". Some of the SKPM measurements were performed at Shandong University, supported by the National Natural Science Foundation of China Grant 62074093. T. H. also acknowledges support from the Qilu Young Scholars Program of Shandong University.

Author contributions

C. D. F. designed and guided the research program. T. H. grew single crystals, fabricated the devices, and performed measurements and analysis. M. S., R. R., and F. W. synthesized the Cl₂-NDI materials, performed UV/Vis/NIR spectroelectrochemistry, and contributed to the scientific discussion of the results. P. P. R. and Y. W. simulated the SKPM results. T.H. and C.D.F. wrote the manuscript with input from all authors.

Additional information

Supplementary information is available in the online version of the paper. Reprints and permissions information is available online at www.nature.com/reprints.

Correspondence and requests for materials should be addressed to T.H. and C. D. F.

Competing financial interests

The authors declare no competing financial interests.

Figures

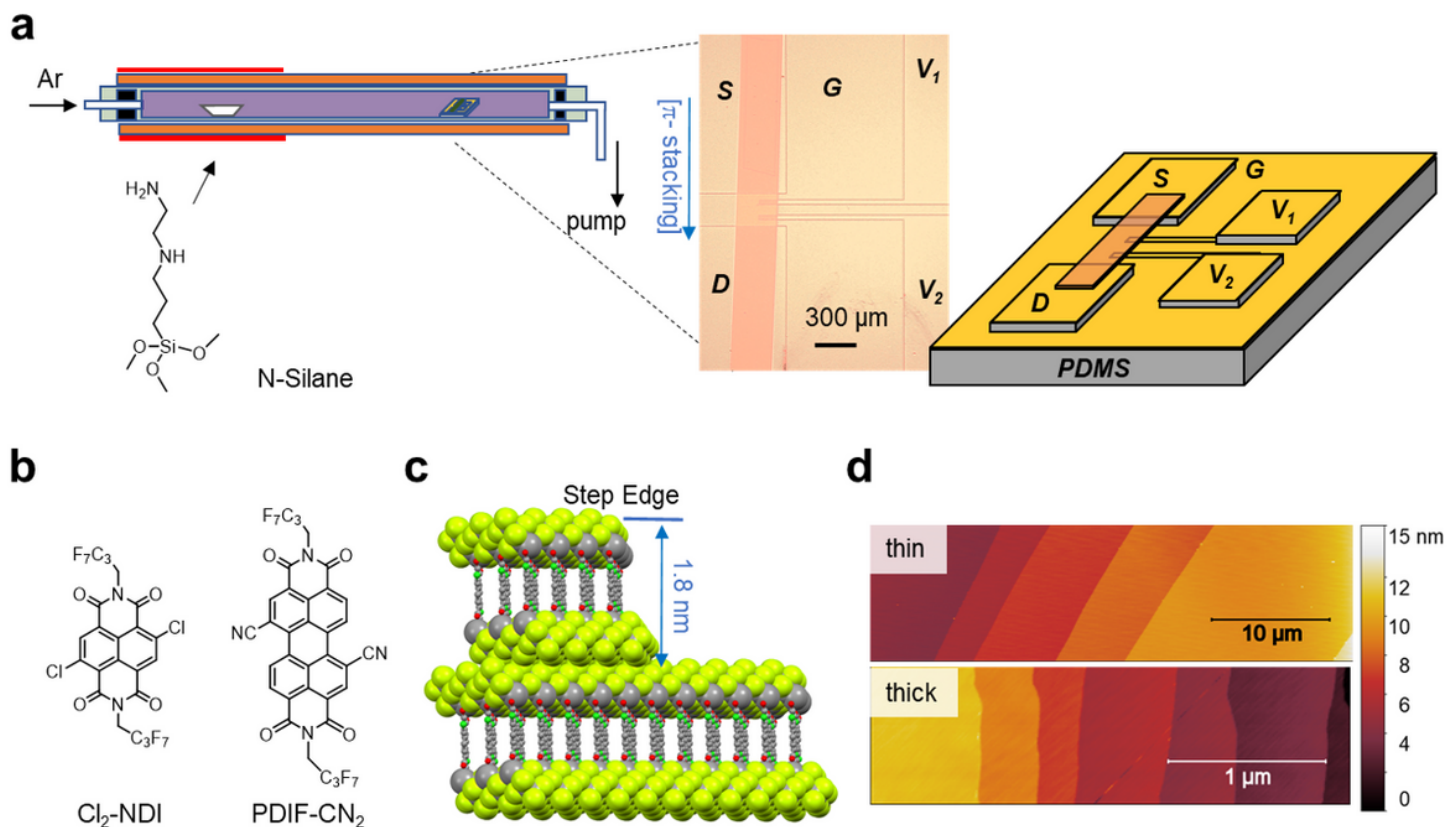


Figure 1

Chemical doping of Cl₂-NDI and PDIF-CN₂ single crystals by exposure to N-silane vapor. a, Schematic diagram of the set-up for chemical doping as well as optical micrograph and scheme of a four terminal vacuum-gap FET on Au-coated PDMS. The chemical structure of the N-silane dopant is shown. S, D, G represent the FET source, drain, and gate electrodes, respectively. V₁ and V₂ are two voltage sensing channel electrodes. b, Molecular structures of Cl₂-NDI and PDIF-CN₂. c, Side view of the crystal packing in the 1.8 nm thick (001) planes of Cl₂-NDI. A step-edge is depicted showing how the pi-system of the Cl₂-NDI molecules at the edge is exposed. The peripheral fluoroalkyl-chains of the Cl₂-NDI molecules are drawn in a space-filling format. Pi-stacking of the Cl₂-NDI aromatic cores facilitates electron transport within the (001) planes. PDIF-CN₂ has a similar packing structure but a different molecular tilt angle within the (001) planes. d, AFM topography images of the step density for Cl₂-NDI single crystals with crystal thicknesses of 3 μm (top) and 40 μm (bottom), respectively. Note the difference in the scale bars.

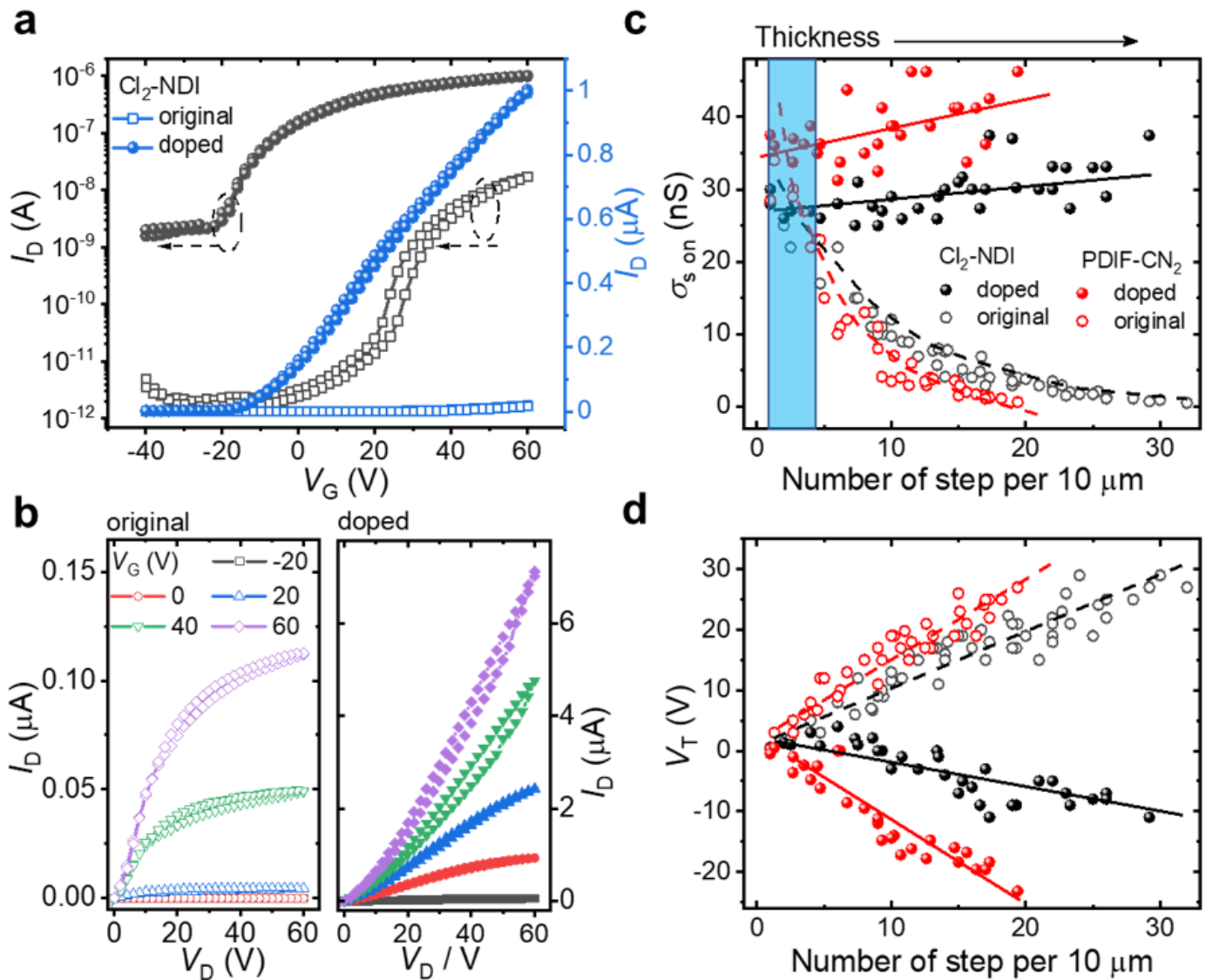


Figure 2

Impact of doping on n-type single crystal FET characteristics. a, FET I_D - V_G characteristics for a thick (47 μ m) Cl₂-NDI crystal with high step density before (open squares) and after (solid circles) exposure to N-silane vapor (100 μ L for 1 h; see Methods). $V_D = 10$ V. The thickness and step density of the single crystal are 47 μ m and 29 steps/10 μ m, respectively. b, Corresponding I_D - V_D characteristics for the same single crystal FET before (left) and after (right) doping. c,d, Doping effect on σ_s (c) and V_T (d) as a function of crystal step density for scores of Cl₂-NDI (black) and PDIF-CN₂ (red) crystals. σ_s is extracted at fixed $V_G = 60$ V and $V_D = 10$ V.

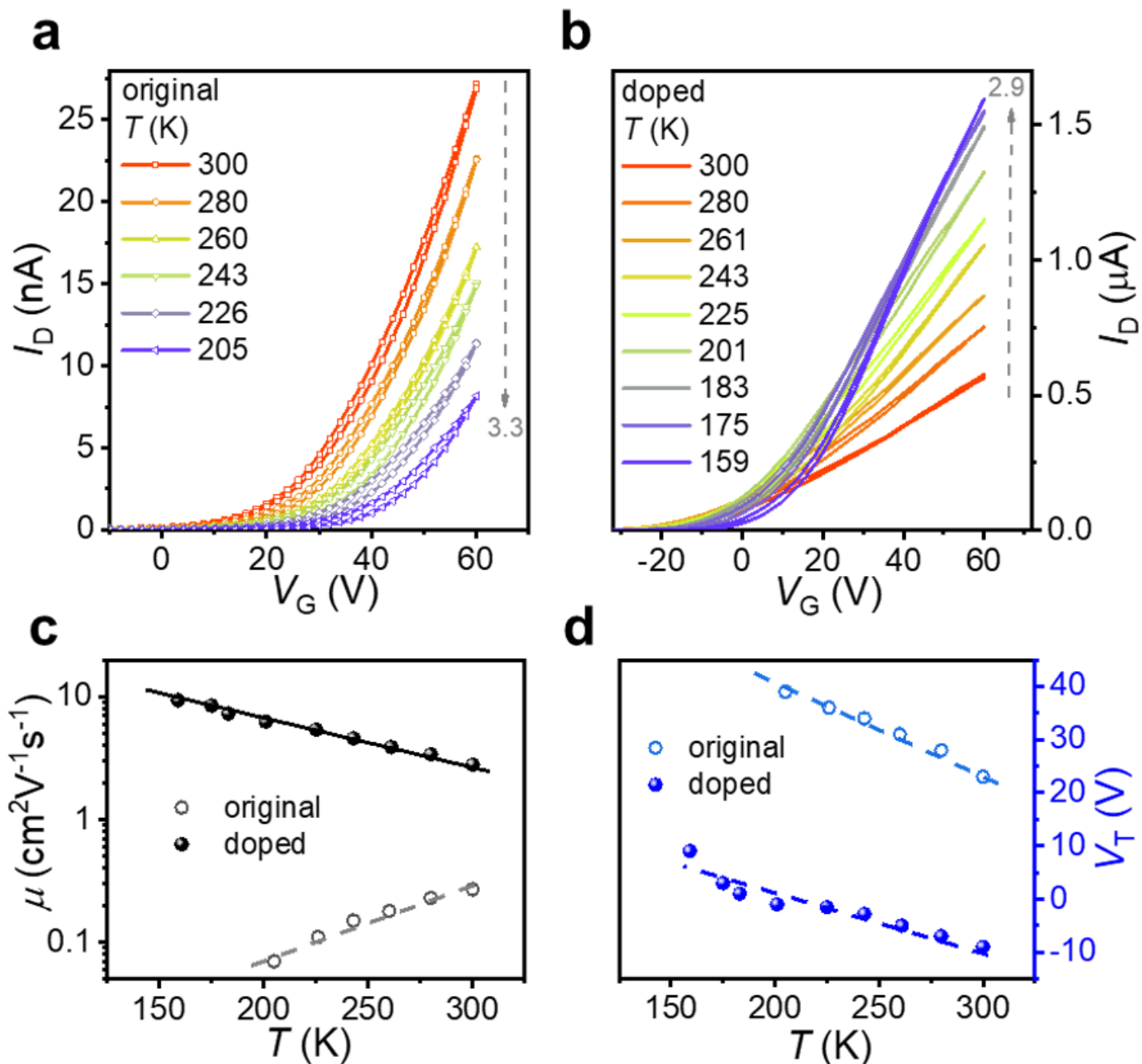


Figure 3

Impact of doping on the temperature dependence of electron transport. a, b, Temperature-dependent I_D - V_G characteristics ($V_D = 10$ V) for an individual thick Cl2-NDI crystal FET before (a) and after (b) doping. c, d, Corresponding behavior of μ (c) and V_T (d) vs temperature. Channel dimensions: $L=300$ μm , $W=490$ μm . The step density is ~ 25 steps/ 10 μm . Mobility is extracted from linear fits to the I_D - V_G characteristic at $V_G = 60$ V.

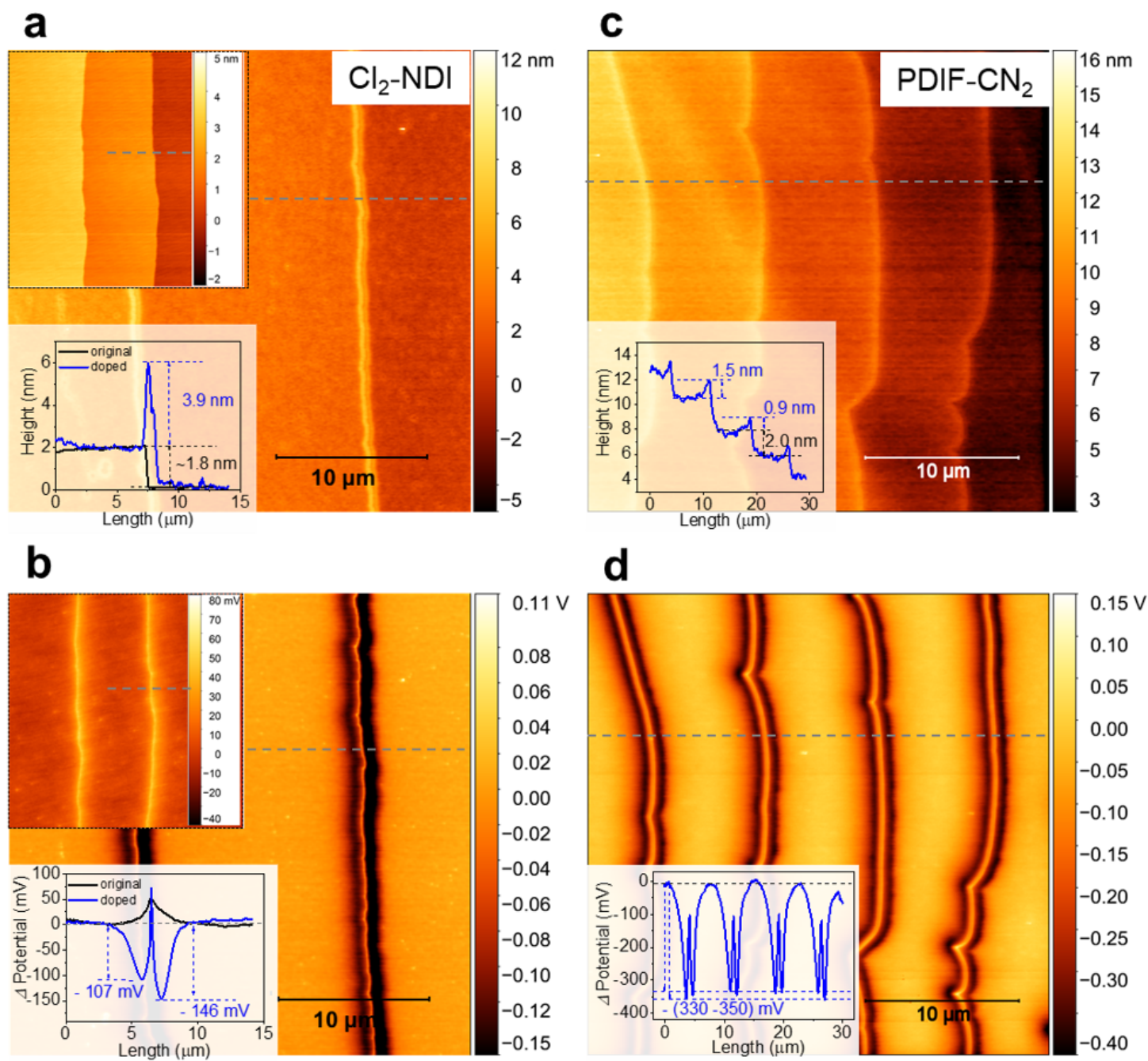


Figure 4

AFM height and SKPM potential images of doped crystals. a,b, AFM topography (a) and SKPM potential (b) images of a doped Cl₂-NDI single crystal. Inset to a: AFM height image of the original crystal and the comparison of height profiles before and after doping along the gray dashed lines. Inset to b: potential image of the original crystal and the comparison of potential profiles before and after doping along the gray dashed lines. c,d, AFM topography (c) and SKPM potential (d) images of a doped PDIF-CN₂ single crystal. Inset to c and d: corresponding height and potential profiles along the gray dashed lines, respectively.

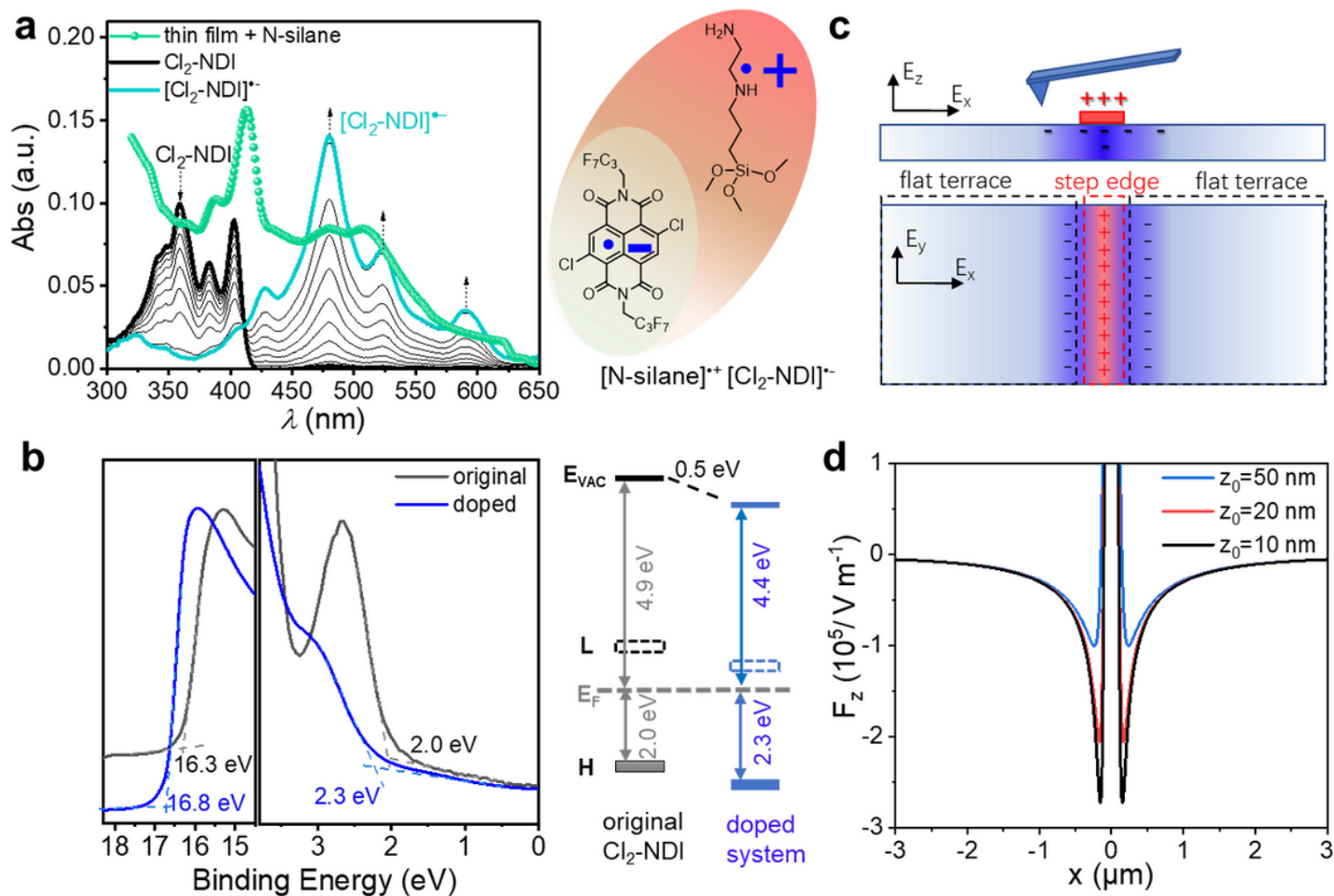


Figure 5

Spectroscopic evidence for doping and computational simulation of the SKPM experiment. a, UV/Vis absorption spectra for a thin film of Cl₂-NDI exposed to N-silane in comparison to the spectroelectrochemical reduction of Cl₂-NDI in CHCl₃ solution to [Cl₂-NDI]^{•-} radical anion. b, UPS measurement of a Cl₂-NDI single crystal (with a very high step density) before and after doping (left) and corresponding energy level line-up for the pristine and n-doped systems (right). The doped crystal has a smaller work function because of the positive ionization of surface-confined donors; the increased HOMO-to-EF offset is consistent with n-type doping. c, Scheme of the space charge distribution along a crystal step edge due to positively ionized donors and the associated electron atmosphere. An experimentally estimated density of positively charged donors is the basis for a finite element simulation of the potential and electric field (see Supplementary Information). d, Simulated profile of the z-component of the electric field (F_z) across the crystal step assuming a spherical SKPM tip with a 50 nm radius scanning at heights of 10, 20, and 50 nm above the crystal surface, as indicated. The simulated F_z profile qualitatively matches the potential profiles in Figure 4b,d.

Supplementary Files

This is a list of supplementary files associated with this preprint. Click to download.

- [SupplementaryInformation.docx](#)